Macromolecules

ARTICLE

pubs.acs.org/Macromolecules

Role of Borderline Solvents to Induce Pronounced Extended-Chain Lamellar Order in π-Stackable Polymers

Li-Hong Zhao,[‡] Rui-Qi Png,[‡] Jing-Mei Zhuo,[†] Loke-Yuen Wong,[‡] Jie-Cong Tang,[†] Yuan-Si Su,[‡] and Lay-Lay Chua[†,‡,*]

[†]Department of Chemistry, National University of Singapore, Lower Kent Ridge Road, Singapore S117543, Singapore

[‡]Department of Physics, National University of Singapore, Lower Kent Ridge Road, Singapore S117542, Singapore

Supporting Information

ABSTRACT: Thin films of poly[2,5-bis(3-tetradecylthiophen-2-yl)thieno-[3,2-*b*]thiophene] (C_{14}–PBTTT) exhibit a monolayer-terraced morphology that indicates a pronounced lamellar order with π-stacks of extended polymer chains. Previously this remarkable state of order was thought to be promoted by the interdigitation of alkyl side chains between the lamellae during cooling from the liquid-crystalline (LC) phase. Here we establish that the key to this ordering in fact is the formation of unentangled π-stacks of extended polymer chains in dilute solutions of chlorobenzene (CB) or 1,2-dichlorobenzene (*o*-DCB), which though routinely used as the "best" solvents are in fact borderline solvents. Film formation causes these π-stacks to deposit substantially oriented in the film plane, while the subsequent anneal and cool from LC phase accentuates this incipient order to develop the monolayer-terraced morphology. This mechanism is supported by the following lines of evidence. (i) Hydrodynamic and viscometry measurements respectively of the Kuhn segment length and Mark–Houwink–Sakurada exponent of PBTTT reveal that CB is a near-Θ solvent, and PBTTT is significantly stiffer than regioregular polythiophene. (ii) Solution-state UV–vis spectroscopy reveals an early coil → rod transition in highly dilute solutions, which gives rise to unentangled π-stacks. (iii) Solid-state UV–vis spectroscopy, atomic force microscopy and variable-angle spectroscopic ellipsometry together reveal the as-deposited π-stacks are already substantially oriented in the film plane. We further demonstrate that this monolayer-terraced morphology can also be induced in regioregular poly(3-hexylthiophene) films using a borderline solvent mixture of chlorobenzene and mesitylene, and in very dilute CB where the incipient π-stacks do not entangle. Therefore, this dilute π-stacking mechanism is general. Processing with a borderline solvent or solvent additive thus provides a general route to obtain superior supramolecular order in π-stackable conjugated polymers.

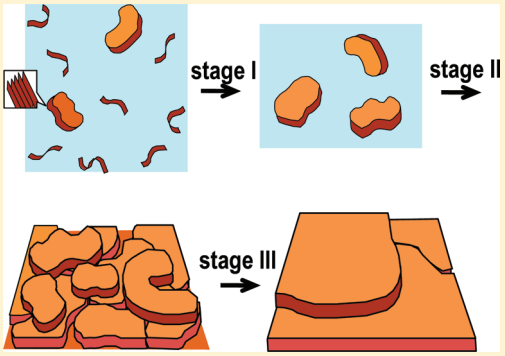

I. INTRODUCTION

The polymer chains of PBTTT and regioregular poly(3-alkylthiophene)s (rrP3ATs) are known to organize into lamellae, i.e., layers of π–stacked polymer chains separated by alkyl side-chains.[1−5] This has been confirmed by wide-angle X-ray scattering (WAXS) which shows both (*h*00) reflections that correspond to lamellar periodicity, and (*k*0) reflections that correspond to π-stacking periodicity within the layers.[6−8] Previously, the (*k*0) reflections have also been denoted (0*k*0) to suggest the presence of a 3D lattice, which is in doubt now. Otherwise the film morphologies of these two families of polymers differ rather remarkably.

Regioregular poly(3-hexylthiophene) (rrP3HT), which has been one of the most well-studied π-stacking polymers, exhibits a rich dependence of film morphology on molecular weight (MW), regioregularity and processing solvent.[2,9−17] Nevertheless the underlying lamellar order is typically characterized by chain-folding or fringed-micelle organization. Low-MW rrP3HTs usually give folded-chain fibres,[9−13] wherein each fiber comprises twice- or thrice-folded polymer chains oriented perpendicular to the π-stacking direction.[9,15,16] The required tight chain-folding involves adoption of the s-*cis* conformation by several adjacent thiophene rings, which has been found by scanning tunneling microscopy.[18] In contrast, high-MW rrP3HTs usually give continuous films with a nodular morphology when spin-cast from the usual solvents such as tetrahydrofuran and chloroform, but also chain-folded fibers if they are dried slowly[14,15] or from poor solvents,[16,19] or after extensive solvent–vapor annealing.[20] Fiber networks despite their apparently higher crystallinity often show severe carrier trapping and hence have not produced good field-effect transistors (FETs).[21] The polymer lamellae in continuous films appeared to be embedded in a fringed-micelle supramolecular structure in which the polymer chains pass through both the π-stacked lamellae and the surrounding amorphous matrix, as suggested by high-resolution transmission

Received: May 25, 2011
Revised: September 20, 2011
Published: November 29, 2011

electron microscopy and the characteristic Hoffman−Weeks crystal-thickening effect.[22,23]

In marked contrast, alkyl-substituted PBTTTs usually give the monolayer-terraced morphology when deposited from *o*-DCB or CB, which indicates the formation of well-ordered π-stacks of extended polymer chains.[7,24] Both the chain-folding and fringe-micelle motif which are less conducive to macroscopic charge transport do not occur to any significant extent in PBTTT films. This leads to an unusually pronounced lamellar ordering that has been thought to account for its improved FET hole mobility μ_{FET} over that of rrP3HT. However we have recently pointed out that the π-stacks are also closer in C_{14}−PBTTT (π...π-spacing, d = 3.63 Å) than in rrP3HT (d = 3.76 Å), which improves its stability to photodoping,[6] and possibly also its interchain coupling and field-effect mobility (μ_{FET}).

The question that we wish to address here is what causes the pervasive π-stacking of extended polymer chains in PBTTT but not in rrP3AT? The answer to this question will reveal important design and/or processing guidlines to further improve the supramolecular order of π-stacking polymers. This will enable new phenomena to be observed. For example, we have recently established for well-ordered PBTTT films the existence of a ring-twist transition[25] and of a localization−delocalization transition of its polarons.[25]

Previously the superior lamellar order in PBTTT has been attributed to interdigitation of ordered alkyl side-chains between the π-stacked lamellae as the polymer cools from the LC phase, which somehow does not occur in rrP3AT,[8,26−28] perhaps due to the lower and more favorable chain density in the former.[27,29] However we have recently established that the tetradecyl side chains of C_{14}−PBTTT are substantially disordered at room temperature[30] just as in rrP3HT[31] in a typical polydispersed material. The *gauche* fraction is significant even at cryogenic temperatures, and increases continually above the dynamic disorder onset temperature T_{dis} of *ca.* 220 K.[30] Therefore, the superior order in PBTTT cannot be driven by side-chain crystallization.

In this report, we show through a systematic study of different MWs of C_{14}−PBTTT that the origin is the early π-stacking of the polymer chains to give extended chain aggregates in dilute solutions. In section II, we describe the experimental details. In section IIIA, we report ^{1}H NMR results that provide the true MW of these polymers and lay the foundation for hydrodynamic measurements. In section IIIB, we report viscometry and gel-permeation hydrodynamic results for the Kuhn segment length and Mark−Houwink−Sakurada exponent that reveal the PBTTT chains exist as (nearly) random coils in highly dilute CB solutions, but CB (and also *o*-DCB) is a borderline solvent for PBTTT. In section IIIC, we report variable-temperature and variable-concentration solution-state UV−vis spectroscopy that reveal an unusually early coil→rod transition of the PBTTT chains in dilute solutions. This forms π-stacked aggregates in their extended-chain conformation. The phase diagram of the random-coil → rigid-rod transition is consistent with a simple stepwise π-stacking association equilibrium model. In section IIID, we show that atomic force microscopy (AFM) indeed provides evidence for the deposition of these extended-chain aggregates that are primarily oriented in the film plane. In section III, parts E and F, we use solid-state UV−vis spectroscopy and variable-angle spectroscopic ellipsometry (VASE) respectively to show that the in-plane orientation order of the film does not further improve with annealing to the LC phase. Therefore, the film is already substantially ordered in-plane as-deposited, and the subsequent anneal and cool from the LC phase only improves this incipient order, but is not primarily responsible for it. In section IIIG, we summarized our mechanism in a cartoon. In section IIIH, we show that this is general by inducing the formation of extended-chain π-stacked lamellae also in rrP3HT, a material that is previously noted for chain-folded fibers and fringed-micelle lamellae, but not extended-chain lamellae.

In a way, this phenomenon of borderline-solvent induced π-stacking is not surprising. However its elucidation here as the formation mechanism of extended-chain π-stacks which can deposit to give practical films with superior lamellar order reveals that processing plays an even more central role than what was previously realized. Instead of focusing on good solvents as is the current practice, one should use borderline solvents to induce the best supramolecular order in π-stacking conjugated polymer films. Finally, this mechanism may also underpin the improved order found when a bad solvent additive is introduced into the processing of blends of polymer with phenyl-C_{61}-butyrate methyl ester (PCBM) that are widely investigated for organic solar cell applications.[32,33]

II. EXPERIMENTAL SECTION

Synthesis of PBTTT Polymers. The PBTTT polymers were synthesized following the McCulloch route using Stille coupling,[7] but with thermal instead of microwave heating. Recrystallized 5,5′-dibromo-4,4′-bis(tetradecyl)-2,2′-bithiophene (purity >99.8%; 1000 mg, 1.40 mmol) was mixed with recrystallized 2,5-bis(trimethylstannyl)thieno[3,2-b]thiophene (purity >99.8%; for **P22**, 650 mg (1.40 mmol); **P11**, 890 mg (1.27 mmol); **P6**, 541 mg (1.16 mmol); **P3**, 433 mg (0.93 mmol)), tris(dibenzylideneacetone)dipalladium (0) (26 mg, 2 mol equiv%), and tri(*o*-tolyl)phosphine (68 mg, 16 mol equiv%) in a round-bottom flask, and flushed with N_2. [Notation: In **P***n*, *n* denotes the true number-average degree-of-polymerization established by ^{1}H NMR, see main text.] Chlorobenzene (CB, 24 mL) was added also under continuous N_2 flow at room temperature, and then heated with stirring to 130 °C (bath temperature) for 20 h. The polymers formed were then nominally end-capped with trimethylstannylbenzene (**P22**, 25 μL (0.14 mmol); **P11**, 50 μL (0.28 mmol); **P6**, 100 μL (0.56 mmol); **P3**, 190 μL (1.07 mmol)) and heated at 130 °C for another 20 h. For **P22**, bromobenzene (28 μL, 0.28 mmol) was also added and heated for another 20 h to encap the trimethylstannyl ends. The reaction mixture was cooled to 50 °C, and the polymer was precipitated into a stirred mixture of MeOH (200 mL) and concentrated HCl (15 mL) at room temperature. The precipitate was filtered and Soxhlet extracted with MeOH and acetone for 24 h each in the dark and under nitrogen to obtain the purified material. ^{1}H NMR confirmed the purity of the final products. We also separately prepared a **P15** material.

General Film Preparation. The native silicon oxide substrates were cleaned by an SC-1 recipe (H_2O:H_2O_2:NH_4OH = 10:2:0.5; 75 °C, 30 min), followed by oxygen plasma (10 min), and then silylated with hexamethyldisilazane (HMDS) in the vapor phase (hot plate 120 °C, 10 min). 10 mg mL^{-1} PBTTT in CB solutions were heated at 85°C (30 min, then 30 min cooled down to room temperature) and spin-coated on these substrates to give a 30 nm-thick PBTTT films.

Gel Permeation Chromatography. Gel permeation chromatography (GPC) was conducted on a thermo-regulated column set (Jordi Gel DVB) using a differential refractometer detector (Waters 2414) and toluene as eluent (flow rate, 0.35 mL min^{-1}). Column was calibrated using polystyrene (PS) MW standards from 2.6k to 190k.

UV−Vis−NIR Absorption Spectroscopy. Absorption spectra were measured using a diode-array UV−vis spectrograph (DW1024, Ocean Optics). Solid-state UV−vis−NIR spectra were collected on 30 nm-thick films spincast on fused silica substrates, and after annealing

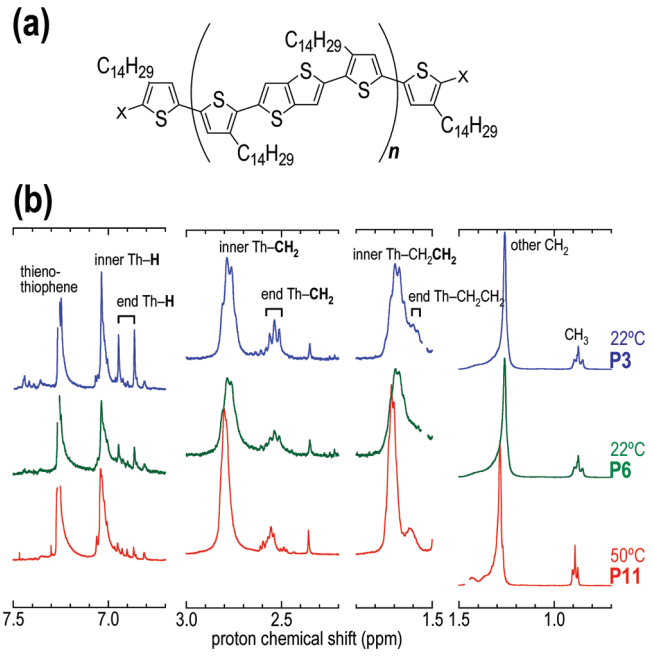

Figure 1. Poly(2,5-bis(3-tetradecylthiophen-2-yl)thieno[3,2-b]thiophene) (PBTTT). (a) Chemical structure giving the meaning of the degree-of-polymerization n in **P*n***. (b) End-group analysis by ^{1}H NMR.

at 120 and 150 °C (10 min each, then cooled to room temperature). Solution-state spectra were collected in CB through a 1.0 cm-path length solution cuvette for dilute solutions, and through thin liquid films held between two fused silica plates using photolithography-patterned spacers to define the path length (2−100 μm) for concentrated solutions. The thin-film cell was briefly annealed at 75 °C on hot plate, and then cooled to room temperature just before measurement. No spectra evolution occurred over the ensuing 5−10 min, therefore pseudo-equilibrium was attained.

Variable Angle Spectroscopic Ellipsometry. Variable-angle spectroscopic ellipsometry (VASE) was conducted on an M-2000 ellipsometer (J. A. Woollam) over the wavelength range 700−1000 nm and at three incidence angles (55.0°, 60.0°, 65.0°). 25 nm-thick spin-cast films were measured at room temperature after spin-casting from CB solutions, and after annealing at 150 °C (15 min, then cooled to room temperature). A three-layer optical model comprising the Si substrate, SiO_2 native oxide layer and polymer film was used to model the experimental (Δ,Ψ) data. The optical constants in the transparent region above 750 nm can be adequately fitted by a Cauchy function of the form: $n(\lambda) = A + B/\lambda^2 + C/\lambda^4$. The fitted film thicknesses were in excellent agreement (±5%) with profilometer values.

Atomic Force Microscopy. Atomic force microscopy (AFM) images were collected in air by tapping mode using a Dimension 3000 Nanoscope instrument with silicon cantilevers. 30 nm-thick films were spin-cast from CB solutions onto HMDS-treated silicon oxide substrates, and imaged before and after annealing above their liquid-crystalline phase transition temperatures (hot plate, 10 min) in the N_2 glovebox.

Intrinsic Viscosity Measurement. Intrinsic viscosity measurement was performed on a Viscolab 450 (Cambridge Viscosity) laboratory viscometer. Variable concentrations of PBTTT solutions (1, 2, 3, and 4 mg mL^{-1}) in CB were prepared at 85 °C (30 min, then 30 min cooled to room temperature) before measurement.

III. RESULTS AND DISCUSSION

We have synthesized a series of C_{14}−PBTTTs with different number-average chain lengths n in geometric steps between 3 and 22 (Figure 1a) by controlling the monomer feed ratio. These polymers are denoted **P*n*** accordingly to emphasize their degree-of-polymerization as the fundamental determinant of their properties. The usual practice of specifying polymers by their MW would emphasize the effect of the side-chains in these "comb" polymers. The value of n was determined accurately by ^{1}H NMR end-group analysis. The true number-average MW M_n corresponding to this n range is 2600−16000. The other parameters such as the theoretical n_{theo} from feed ratio, true weight-averaged chain-length n_w, and average number of π-electrons per chain, are given in Table 1. The tetradecyl side-chain was chosen for processability, since the reported dependence of μ_{FET} on side-chain length between 10−14 is very weak.[7]

Table 1. Useful Parameters Extracted from End-Group Analysis ^{1}H NMR[a]

	P22	P11	P6	P3
$n_{theo} = 1/1 - r$	>150	11	5.8	3.0
n	22	11 ± 2	5.5 ± 0.3	2.9 ± 0.1
n_w	37	19 ± 3	8.8 ± 0.5	4.1 ± 0.1
M_n	16k	8.2k	4.3k	2.6k
no. of π electrons	320	160	86	48
M_n*/ M_n	2.18	2.31 ± 0.14	2.28 ± 0.04	2.5 ± 0.02

[a] n is the true number-average repeat unit determined by end-group analysis ^{1}H NMR; n_{theo} is the theoretical number-average repeat unit where r is the feed ratio; n_w is the true weight-average chain-length obtained by [n × polydispersity]; M_n is the true number-average molecular weight given by [(n × molar mass of repeat unit) + molar mass of end unit). Mn* is the apparent number average molecular weight based on PS-standardized GPC.

Although the M_n values here appear to be low, **P22** is in fact the longest chain length that can be synthesized in hot CB owing to solubility limits. It is also similar to those reported elsewhere,[34] after taking into consideration the usual PS-standardized GPC reports apparent M_n* values that are 2.5 times of the true M_n (Table 1) due to neglect of chain stiffness. The n range investigated here corresponds to quite large π-electron systems with 48−320 π-electrons because the repeat unit is large. Their optical properties indeed indicate the infinite-chain limit has been reached, e.g., the π−π* absorption gap of **P3** in the solid state lies within 10 meV of **P22**. We have recently investigated the supramolecular organization of these polymers from the chain-length dependence of their T_{dis}, liquid-crystalline (T_k), and isotropic (T_i) phase transitions,[30] and clarified their superior air-stability over rrP3ATs[24,35] derives primarily from a kinetic effect.[6]

A. Determination of the True Molecular Weight. We employed ^{1}H NMR end-group analysis to evaluate n. Since very little has been written about this in the literature, it is worth to describe it in some detail. The PBTTT chain is terminated at both ends by thiophene (Th) units due to excess Th used. These chain-end Th units can be distinguished from the inner Th units by the different deshielding effect on their protons (Figure 1b): (i) The Th−$\mathbf{CH_2}$ protons on the chain-end Th rings occur at δ2.54 ppm (triplet) while those on the inner Th rings occur at δ2.78 ppm (unresolved multiplet). (ii) The Th−**H** proton on the chain-end Th ring occurs at δ6.94 and δ6.86 ppm (singlets, due to the presence or absence of the capping group) while those on the inner Th rings occur at δ7.04 ppm (singlet). The ratio of the integrated intensities of the inner protons to the chain-end

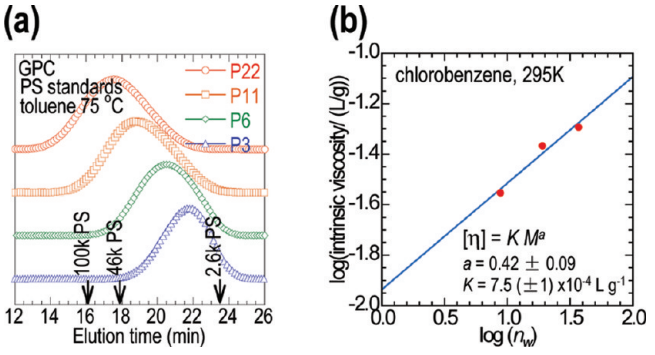

Figure 2. (a) GPC elution characteristics of the PBTTT polymers with peak positions of the polystyrene standards marked. (b) The log−log plot of intrinsic viscosity against the weight-average degree-of-polymerization n_w in chlorobenzene at 295 K and fitted with the Mark−Houwink−Sakurada equation.

protons thus gives n directly. Analysis of both types of protons (Th−**H** and Th−C**H**$_2$) gives the same results. [No monomer signal was detected (<0.01%): bithiophene monomer (6.77 ppm), thienothiophene monomer (7.30 ppm).] We found that the n values obtained are in excellent agreement with theoretical predictions from the monomer feed ratio (Table 1), except for **P22** which is limited by solubility in CB at the polymerization temperature. Therefore, the polymerization reaction is well-behaved.

B. Determination of Kuhn Segment Length and Mark−Houwink−Sakurada Exponent. The solution-state Kuhn segment length ℓ_k and the Mark−Houwink−Sakurada exponent a of the C_{14}−PBTTT polymers were evaluated to determine their properties in highly dilute CB solutions. We chose to study CB rather than *o*-DCB solutions,[8,26−28] because the former has a suitable vapor pressure (12 mmHg at 25 °C) for film formation via spin-casting and inkjet-printing, while the latter is too slowly evaporating (2 mmHg at 25 °C) which often leads to film dewetting. Both CB and *o*-DCB are in fact borderline solvents for C_{14}−PBTTT even though the latter is marginally better (see also section IIIC).

To determine ℓ_k, we first measured the hydrodynamic volume of the PBTTT polymers using the well-established "universal calibration" method, in which the elution time of the polymer through the GPC column gives its hydrodynamic volume that is independent of the nature of the polymer.[36] Therefore, the mean square radius-of-gyration $\langle s_g^2 \rangle$ of the polymer chains can be found by comparing their elution time with those of PS standards (Figure 2a).[37] For a Gaussian chain, this $\langle s_g^2 \rangle$ is related to ℓ_k by

$$\langle s_g^2 \rangle = \frac{1}{6} n_k \ell_k^2 \quad (1)$$

where n_k is the number of Kuhn segments on the chain. This in turn is also related to its contour length by

$$L_c = n_k \ell_k \quad (2)$$

which can be computed from n as shown in Table 2.

The chain-length dependence of $\langle s_g^2 \rangle$ for PS is known from small-angle neutron scattering,[38] from which the $\langle s_g^2 \rangle$ values of the different **Pn** polymers are obtained. Then the ℓ_k values are computed using eqs 1 and 2, and given also in Table 2. We found that the average ℓ_k of C_{14}−PBTTT is 9.0 nm, which

Table 2. Useful Parameters Calculated and Tabulated to Obtain the Kuhn Segment Length ℓ_k[a]

	P22	P11	P6	P3
L_c= 13.8 Å × n	30 nm	15 nm	7.5 nm	4.0 nm
$\langle S_g^2 \rangle^{1/2}$	7.0 nm	4.8 nm	3.2 nm	2.4 nm
$\ell_{k,PBTTT}$	9.8 nm	9.2 nm	8.2 nm	8.6 nm

[a] $\langle S_g^2 \rangle^{1/2}$ is the radius of gyration; L_c is the computed number-average contour length where 13.8 Å is the length of PBTTT repeat unit.

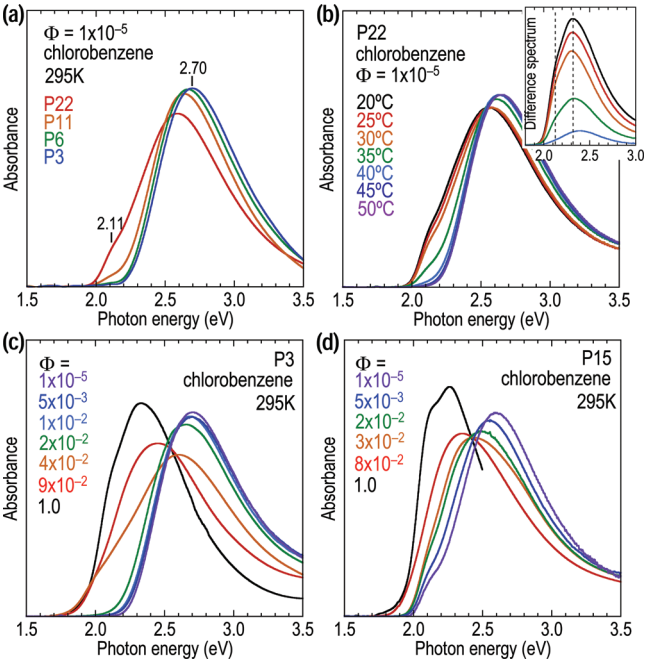

Figure 3. UV−visible absorption spectra of variable-MW PBTTT solutions in chlorobenzene. (a) Different n at a volume fraction Φ of 1×10^{-5} at 295 K. (b) Variable-temperature spectra of **P22** at Φ=1×10^{-5}. Inset shows the spectra of the π-stacked aggregates obtained by taking difference with 45°C spectrum (same color legend). Variable-concentration spectra: (c) **P3** and (d) **P15**, for Φ between 1×10^{-5} and 9×10^{-2}, collected at 295 K. The solid-state spectra (Φ = 1.0) are also shown.

is significantly stiffer than PS (2.8 nm) and even rrP3HT (4.8 nm).[39] The chain persistence length given by $\ell_k/2$ is about three repeat-units long.

To determine a, we first evaluated the zero-concentration intrinsic viscosities $[\eta]$ of the CB solutions at 295 K by a standard dual-line extrapolation: (i) $[\eta] = \lim_{c \to 0} \eta_{sp}$, where the specific viscosity is given by $\eta_{sp} = (\eta - \eta_{solv})/(c\eta_{solv})$, with c as polymer concentration, η as solution viscosity and η_{solv} as solvent viscosity; (ii) $[\eta] = \lim_{c \to 0} 1/c \ln \eta/\eta_{solv}$.[36] We then performed a Mark−Houwink−Sakurada fit using $[\eta] = KM^a$, by plotting $[\eta]$ against the weight-average chain length n_w used to approximate the required viscosity-average chain length (Figure 2b), to obtain slope $a = 0.42 \pm 0.09$, and intercept $K = 7.5\ (\pm 1) \times 10^{-4}$ L g^{-1}.

These results demonstrate that: (i) C_{14}−PBTTT chains in highly dilute CB solutions (1−4 mg mL^{-1}) adopt a random-coil rather than a rigid rod (a = 2) conformation; and (ii) CB is a near-Θ solvent for C_{14}−PBTTT ($a \approx 0.5$). A Θ solvent is the borderline solvent for the polymer, because very long polymer chains cannot dissolve in a solvent that is poorer than the Θ solvent. For

comparison, rrP3HT gives a = 0.58 in THF which is thus a moderately good solvent.[39]

C. The Coil → Rod Transition Onset in Dilute Solutions: Variable-Concentration and Variable-Temperature UV−Vis Spectrometry. We found that a borderline solvent causes the coil → rod π-stacking transition of the polymer to occur even in dilute solutions where the polymer volume fraction Φ is small. This turns out to be key to the formation of unentangled 2D polymer π-stacks of the fully extended chain conformation.

Figure 3a shows the solution-state UV−vis absorption spectra of **P3**−**22** at $\Phi = 1 \times 10^{-5}$, i.e., *ca.* 0.01 mg mL^{-1}, which is close to "infinite" dilution. The band maximum at 2.6−2.7 eV arises from the conformationally disordered chains which we have also previously denoted the δ state.[24] The band maximum red-shifts little from 2.7 eV in **P3** to 2.6 eV in **P22**, but the red shoulder at 2.1 eV grows markedly. This shoulder indicates the presence of π-stacked aggregates because it falls in the same region as the dominant absorption of the π-stacks in the film.

The temperature dependence of the equilibrium between the disordered δ-state and the π-stacked state is shown for **P22** in Figure 3b. The intensity of the π-stacked state diminishes with increasing temperature and disappears at 45 °C, above which the band shape becomes similar to that of **P3**. The thermal coefficient of the band maximum (1.2 meV K^{-1}) is also similar to that of **P3**. It is therefore clear that at elevated temperatures, C_{14}−PBTTT exists in a well-defined disordered state. We thus use the 45 °C-spectrum as reference for this state. By appropriately scaling and subtracting its contribution to the spectra at lower temperatures, we obtained the difference spectra for the π-stacked state, as shown in the inset of Figure 3b. These spectra show the characteristic features (2.13 and 2.32 eV) of the β-state known in the film.[24] The temperature dependence shows that this state is formed exothermically, while the pseudoisosbestic point at 2.54 eV suggests a simple equilibrium between the δ-state and this π-stacked state.

To determine the concentration dependence of this equilibrium, we measured the spectra as a function of Φ, as shown in Figure 3, parts c and d, for **P3** and **P15**, respectively. In order to cover a wide Φ-range spanning 5 orders of magnitude from 1×10^{-5} to 9×10^{-2} (with $\Phi = 1.0$ given by the solid-state), we used a series of home-built liquid cells with lithographically patterned spacers to set the separation (2−100 μm) between two fused silica plates to keep the peak absorbance between 0.5−2.

The results reveal a strong Φ-dependence with a very early onset in dilute solutions. This onset further decreases with increasing chain length. For **P3**, the spectrum red shifts only above $\Phi \approx 1 \times 10^{-2}$, but for **P15**, this occurs at $\approx 2 \times 10^{-3}$. The strong concentration dependence suggests the π-stacks are formed primarily by interchain aggregation with a strong chain-length dependence. However because the longest chains (**P11** and above) show a π-stacked state even at "infinite" dilution, there is also a small fraction of folded chains. This suggests that the fraction of π-stacks grow from the very initial stages of solution drying, and not just as the point of incipient dryness. Again the pseudoisosbestic point at 2.5 eV shows that the equilibrium is dominated by only two spectroscopically distinct species, the δ- state and the π-stacked state.

This suggests the process can be quantitatively modeled in a simple way. First, each solution-state spectrum $S(E)$ was fitted with the δ-state spectrum $S_{coil}(E)$ to extract the π-stacked aggregate spectrum $S_{agg}(E)$: $S_{agg}(E) = S(E) - \xi S_{coil}(E)$, where

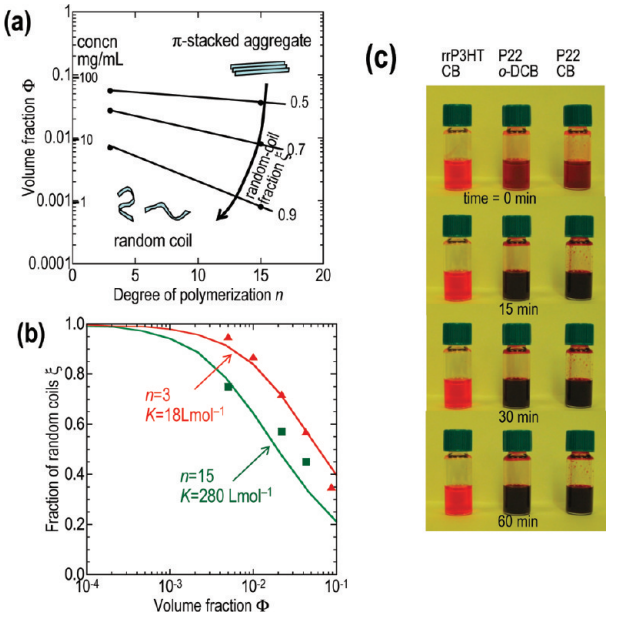

Figure 4. (a) Phase diagram showing the random-coil iso-fraction contours (ξ) of 0.5, 0.7 and 0.9, plotted against polymer volume fraction (Φ) and chain length n. (b) Dependence of ξ on Φ. Solid symbols (red ▲, green ■) are experimental data and solid lines are fits to the stepwise association equilibrium model. (c) Photographs of 5 mg mL^{-1} rrP3HT and **P22** solutions at the indicated times after removal from the 85 °C hot well in the N_2 glovebox. Key: left panel, rrP3HT in CB; middle panel, **P22** in *o*-DCB; right panel, **P22** in CB.

ξ is a scaling factor that gives the fraction of disordered chains. This yields ξ as a function of Φ for different n. When constant fractions of the disordered state are plotted (e.g., for ξ = 0.9, 0.7, and 0.5) against (Φ, n) we obtained a simple phase diagram of the π-stacking aggregation (Figure 4a). The volume fraction over which the disordered δ-state is stable diminishes with increasing chain length. At the typical solution concentration used for film deposition of 10 mg mL^{-1}, 10−30% of the chains are already π-stacked depending on n.

We then modeled the π-stacking as stepwise association equilibria as follows:

$$P_1 + P_1 \rightleftarrows P_2;\ K_2 = \frac{c_{P_2}}{c_{P_1}^{\,2}}\ln;\ K_2 = -\frac{\Delta G_2}{RT} = -\frac{\Delta H_2}{RT} + \frac{\Delta S_2}{R}$$

$$P_1 + P_2 \rightleftarrows P_3;\ K_3 = \frac{c_{P_3}}{c_{P_1} c_{P_2}}\ln;\ K_3 = -\frac{\Delta G_3}{RT} = -\frac{\Delta H_3}{RT} + \frac{\Delta S_3}{R}$$

$$P_1 + P_{j-1} \rightleftarrows P_j;\ K_j = \frac{c_{P_j}}{c_{P_1} c_{P_{j-1}}}\ln;\ K_j = -\frac{\Delta G_j}{RT} = -\frac{\Delta H_j}{RT} + \frac{\Delta S_j}{R}$$

where j is the π-stacked aggregate size (where P_1 denotes the isolated chain), and the usual thermodynamic quantities (ΔH_j, ΔS_j, and ΔG_j) and stepwise formation constants (K_j) are written for molar concentrations c_j. Assuming that all stepwise association quantities are identical, i.e., $\Delta H_2 = \Delta H_3 = ... = \Delta H_j = \Delta H$; and $\Delta S_2 = \Delta S_3 = ... = \Delta S_j = \Delta S$; and so $\Delta G_2 = \Delta G_3 = ... \Delta G_j = \Delta G$; and $K_2 = K_3 = ... = K_j = K$, since the change in enthalpy and entropy for each additional chain added to the π-stack may not differ greatly, we applied mass balance, $n_{P,0} = \Sigma_{j=1}^{\infty} j c_{P_j}$ to obtain the equation: $n_{P,o} = \Sigma_{j=1}^{\infty} j K^{j-1} c_{P_1}^{\ j} = 0$, which

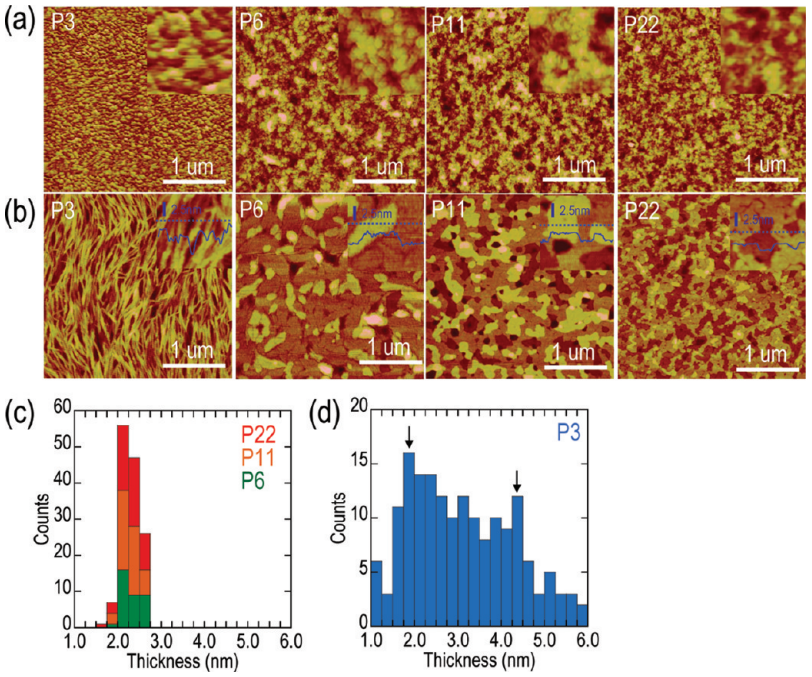

Figure 5. 3 × 3 μm AFM of 30 nm-thick PBTTT films on HMDS-treated silicon oxide substrate (a) before and (b) after annealing to 10 K above the liquid-crystalline phase-transition temperature for 10 min followed by cooling. All insets give zoomed-in 500 × 500 nm images with line profiles that clearly reveal the monolayer step heights after annealing. Thickness histogram of the surface PBTTT layer measured by AFM for (c) **P6**−**P22**, and (d) **P3**. The monolayer step height is 2.2 nm. About 50 measurements for **P6**−**P22** and 150 for **P3** were collected randomly from each images. z-scale is 10 nm.

yields a single parameter K to fit the experimentally observed dependence $\xi(\Phi, n)$.

Two examples of these curves are plotted in Figure 4b, for n = 15 and K = 280 L mol^{-1}; and for n = 3 and K = 18 L mol^{-1}. These give ΔG = −7.1 kJ mol^{-1} for n = 3, and −14 kJ mol^{-1} for n = 15. These K values were chosen to provide best match to experiment (theory, curve; experimental data, symbols). We find that the data is sufficiently well reproduced by this simple model, and thus the coil → rod transition is a π-stacking transition.

Figure 4c shows the solvatochromism of the polymer solutions that illustrates the formation of these π-stacks in dilute solutions of borderline solvents. Three polymer solutions were prepared at a concentration of 5 mg mL^{-1} at 85 °C in the glovebox, and photographed at fixed time intervals after their removal from the hot well: **P22** in *o*-DCB and in CB, and rrP3HT of similar chain length in CB. The rrP3HT solution remains bright orange due to the stability of its δ-state over days, while both the C_{14}−PBTTT solutions turn dark red immediately and black within 15 min, due to π-stacking in solution. Clearly while *o*-DCB may be a slightly better solvent than CB (Supporting Information, Figure S1), both are borderline solvents for C_{14}−PBTTT.

While such a coil → rod transition has been generally known during drastic solvent change,[40,41] when crystallizing from the melt,[42−46] and in the final drying stage of film formation, our result here shows that a borderline solvent can promote its occurance in dilute solutions, where the polymer chains do not entangle with neighboring π-stacks and hence are free to adopt the fully extended conformation. This is a significant departure from previous work that has not been fully appreciated. If the solvent quality is too good, the π-stacks form too late during film deposition, and so their inevitable entanglement prevents the attainment of high order; while if the solvent quality is too bad, the π-stacks precipitate too early as fibers or particles which are also not desirable.

D. Imaging the Deposition of In-Plane-Oriented π-Stacked Aggregates: Atomic Force Microscopy. Figure 5 shows AFM topographic images of 30-nm-thick **P*n*** films spin-cast from 10 mg mL^{-1} CB solutions for different n. The first row of images (Figure 5a) gives the film morphology as-spincast, while the second row (Figure 5b) gives the morphology after annealing to 10−40 K above T_k and cooling. The insets give zoomed-in 500 × 500 nm images. The T_k values for n = 3, 6, 11, and 22 are *ca.* 360, 385, 400, and 435 K respectively, which correspond to melting of the lamellar crystal to the nematic LC phase.[7,30]

The annealed **P3** film shows nanoribbons,[34] with width and height distributions as shown in Figure S2d (Supporting Information) and Figure 5d, respectively. The typical widths of 20−50 nm correspond to 5−10 extended chains, while the height distribution shows a peak at 2.2 and 4.4 nm, corresponding to 1× and 2× of the lamellar spacing. These peaks are broadened because the ribbons may not rest conformally on the underlying ones. The π-stacking direction is clearly in the film plane. The presence of monolayer ribbons here is different from rrP3HT in which the minimum whisker thickness is 2× or 3× of the lamellar thickness.[9−13,15,16] In contrast the annealed **P6** film shows equi-axed nanoplatelets (Figure 5b) with a topmost monolayer island widths of 80−250 nm (*cf.* contour length L_c = 7.5 nm; Figure S2c), and clean monolayer step heights of 2.2 nm (Figure 5c). As n increases to **P11** and **P22**, the annealed film gradually adopts the characteristic monolayer-terraced morphology (Figure 5b) that has been well-known for PBTTT, with the topmost island widths in **P22** (Figure S2a) and **P11** (Figure S2b) still several times of their L_c. This transition from

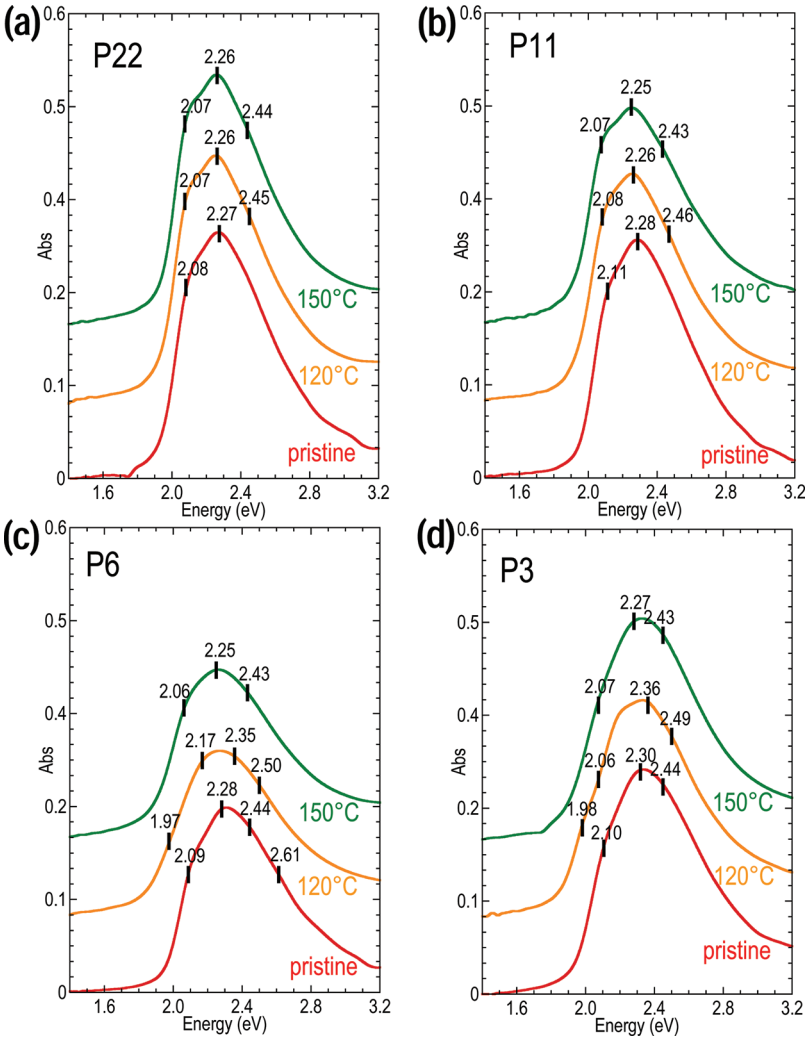

Figure 6. UV−visible absorption spectra of 30 nm-thick PBTTT pristine films deposited by spin-casting on fused silica substrates, before and after annealing to 120 and 150 °C (10 min stepwise). (a) **P22**, (b) **P11**, (c) **P6** and (d) **P3**. Peak positions and shoulders have been marked by taking second-order derivatives of the line shapes.

nanoribbon to terraced morphology has been briefly noted before.[34]

The terraces in **P6**−**22** clearly show domains at various stages of coalescence. Thus, each island terrace is made of subdomains. The key result here is that both the height and width distributions are consistent with the predominance of π-stacked lamellae of extended polymer chains. Only monolayer step heights are observed with no evidence of chain-folding which would give bilayer and higher multiples of the monolayer step heights. Also, the island widths are always substantially larger than L_c.

To obtain further evidence for monolayer π-stacks of extended chains in the *as*-deposited film, we have carefully studied the AFM images before annealing. We found a nodular morphology (Figure 5a) for all *n*, but unlike rrP3HT, comprises islands at least 20 nm wide and *ca.* 2 nm high. This is characteristic of monolayer π-stacks with extended chains that appear to be more or less oriented in the film plane. In some cases, the morphology of these islands is irregular or curved. Examination of the 500 × 500 nm images shows from their distinctive *z*-height layering that these islands are deposited on lower layers of partially or fully coalesced islands.

Therefore, 2D π-stacks are deposited substantially parallel to the film plane. This means the subsequent anneal and cool from the LC phase only acts to improve the incipient lamellar order, which is firmly supported by solid-state UV−vis spectroscopy (section IIIE) and VASE (section IIIF). The inescapable conclusion is the monolayer-terraced morphology of PBTTT films has its origin in the early solution-state π-stacking to give substantially extended-chain aggregates.

E. Confirmation of In-Plane Orientation Order in *as*-Deposited Films: (i) Lack of Significant Change in the Intensity of the π-Electronic Spectrum upon Annealing. Figure 6 shows the solid-state UV−vis spectra of 30 nm-thick **P*n*** films, *as*-deposited and after a 120 and 150 °C anneal, together with the positions of the spectral components marked by taking the second derivative. The use of second derivatives together with Frank−Condon modeling[47] allows the resolution of overlapping vibronic progressions from different π-stacked states which we have previously denoted α-, β- and γ-states.[24] The vibronic members are spaced by 0.18 eV, which corresponds to the mean energy of the three dominant Raman modes (1490, 1414, 1390 cm^{-1}). However each progression is built on a different electronic

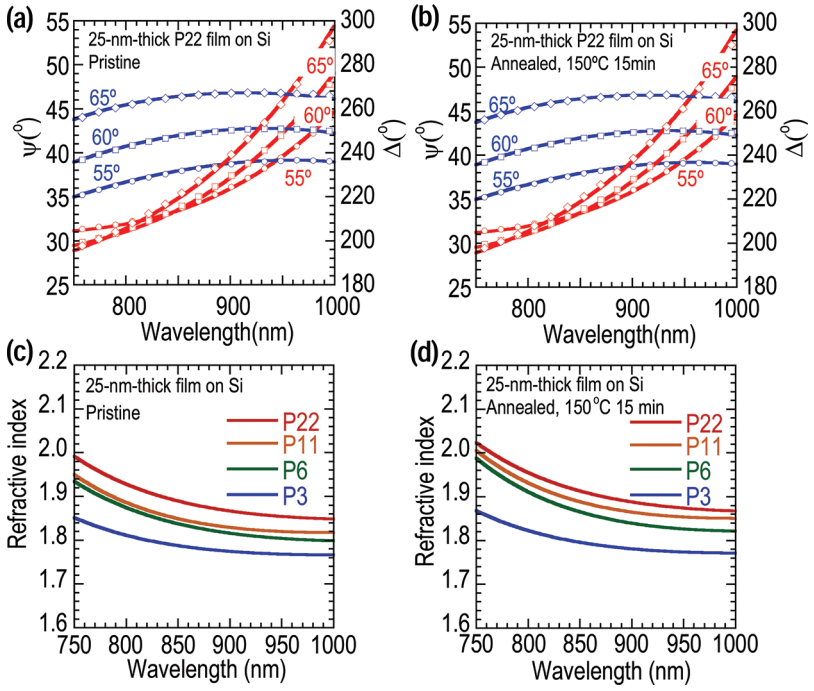

Figure 7. Reflection VASE (Δ,Ψ) spectra for the 25 nm-thick film of **P22** spin-cast onto oxygen plasma-treated silicon oxide substrates, (a) before and (b) after annealing at 150 °C (15 min, N_2 glovebox). Symbols are experimental data, and lines are model. Only 10% of experimental data are shown for clarity (○ = 55°, □ = 60°, ◊ = 65°). The chi-square of the fits are better than 2.5 over all three incidence angles, which indicates the optical model used is reliable. Refractive index spectra of 25 nm-thick PBTTT films modeled from the VASE data, (c) before and (d) after annealing at 150 °C (15 min, N_2 glovebox).

origin (α 2.08; β 2.15; γ 1.94, $\delta \approx 2.3$ eV). Only a tiny red shift (*ca.* 10 meV) was observed after annealing to 150 °C. Also the **P22** and **P11** films exhibit the α-state clearly before and after the annealing, while **P6** and **P3** films show a transient γ-state after the 120 °C anneal.

The key result here is that the $\pi-\pi^*$ absorption band intensity is practically unchanged before and after annealing to the LC phase. Since the $\pi-\pi^*$ transition is polarized along the polymer chain axis,[48] this demonstrates that the average orientation of these chains has not changed, despite the remarkable development of the monolayer-terraced morphology. Thus, it is clear that the *as*-deposited film already comprises polymer chains that are oriented in the film plane.

F. Further Confirmation of In-Plane Orientation Order in *as*-Deposited Films: (ii) Lack of Significant Change in the Effective In-Plane Dielectric Function. As further evidance, we used VASE to measure the in-plane dielectric spectra of the **P*n*** films before and after annealing to the LC phase. No significant change was found. The dielectric spectrum comprises a real component (refractive index) and an imaginary component (extinction coefficient) that are sensitive to orientation anisotropy in the film, since the $\pi-\pi^*$ transition is polarized along the chain axis.[48] By the Kramers−Kronig relation, the dielectric spectrum of the film will become anisotropic even in the transparency region. The advantage of working in this transparency region is its simplicity, since measurement of the refractive index spectrum suffices as the extinction coefficient is zero.

We measured the reflection (Δ,Ψ) spectra of 25- nm-thick spin-cast films of **P*n*** on Si wafers in nitrogen before and after annealing, over the 750−1000-nm transparency region, and at three incidence angles θ = 55.0°, 60.0° and 65.0°. Δ and Ψ are ellipsometric angles related to the ratio of complex amplitude reflection coefficients by $\tilde{R}_p/\tilde{R}s = \Psi\exp(i\Delta)$. We modeled the refractive index spectrum using a standard Cauchy function. The film thicknesses were chosen to be 25 nm to lie within a "sweet spot" in which the film response is strongly weighted by the in-plane response of the film (see the Supplementary discussions in ref 49). We can thus model the data using four optical layers: Si substrate/SiO_2/ film/air, and using isotropic dielectric functions for all the layers. Note that the neglect of film anisotropy under these conditions does not introduce significant error to the modeled in-plane response, simply because the measurements are not sufficiently sensitive to the out-of-plane response, which therefore has to remain unknown.[49,50]Parts a and b of Figure 7 illustrate the excellent quality-of-fit routinely obtained, with chi-square values <2.5.

Parts c and d of Figure 7 plot these in-plane refractive index spectra before and after annealing, respectively. The key observation is that for all chain lengths, these spectra change very little upon annealing. The increment is ≤0.01 units at 1000 nm and ≤0.025 units at 750 nm-wavelength, which is a tiny fraction of the difference between the in-plane and out-of-plane values of these films (≈0.3 and 0.7 respectively at these two wavelengths).[48] In fact, this increment is already fully attained by annealing to 120 °C, and hence has nothing to do with the emergence of the monolayer-terraced morphology at T_k. It can in fact be quantitatively modeled as the elimination of 2−3% void fraction present in the *as*-deposited film.

Therefore, it can be firmly concluded from both VASE and solid-state UV−vis spectroscopy that annealing of the films to their LC phase, which is needed to develop the pronounced monolayer-terraced morphology, has not led to any significant increase

in film anisotropy. This means that the *as*-deposited films are already anisotropic, and the π-stacks are more or less oriented in the film plane throughout the film.

G. Summary of Mechanism: Formation of Unentangled 2D π-Stacked Extended-Chain Aggregates in Dilute Solution. We summarize our mechanism for the lamellar ordering of PBTTT thin films in Figure 8a. This occurs in three stages. In **stage-I**, which occurs in a borderline solvent, the polymer chains π-stack in their extended conformation into "large" 2D aggregates in dilute solution. This is firmly indicated by the measured phase diagram for the coil→rod π-stacking transition. In **stage-II**, these π-stacks are deposited parallel to the substrate plane during film formation, with the polymer chains primarily oriented parallel to the film plane. This is firmly indicated by AFM, solid-state UV−vis spectroscopy and VASE measurements of the films before and after annealing. In the final **stage-III**, when the dried film is annealed to its LC phase and cooled, the π-stacks are melted while retaining their in-plane orientation (i.e., a nematic phase),[30] which allows the lamellar order to reform with improved quality. Throughout this process, the side chains are substantially disordered,[30] do not have to substantially crystallize as widely speculated in the literature.[8,26−28,30]

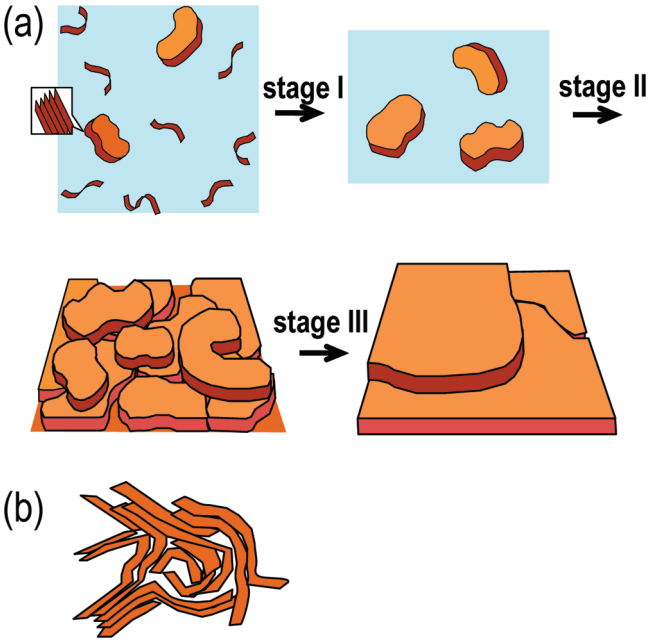

Figure 8. (a) Schematic of the dilute π-stacking mechanism that leads to formation of unentangled π-stacked extended-chain lamellae that give rise to the monolayer-terraced film morphology. This mechanism can be induced by a borderline solvent or in very dilute solutions of a good solvent. (b) Schematic illustration of the morphology of a thick film deposited from a good solvent.

In contrast, in a good solvent, the coil → π-stack transition occurs much later during film formation when the polymer chains inevitably overlap and the neighboring π-stacks become entangled. This prevents the formation of extended-chain π-stacks and their orientation to the film plane. As a result, the film retains a significant amorphous fraction (Figure 8b) and does not develop the monolayer-terraced morphology. Nevertheless, this can be overcome by spin-casting from very dilute solutions where the π-stacks can still be formed sufficiently far apart to avoid entanglement, but at the expense of being able to deposit only ultrathin films. This has now been experimentally demonstrated to induce mono terrace morphology in rrP3HT (section IIIH).

H. Using this Dilute π-stacking Mechanism to Induce the Monolayer-Terraced Morphology in rrP3HT Films. To illustrate the generality of this mechanism, we show that the superior lamellar order can also be induced in rrP3HT films by either processing in a borderline solvent or by forming ultrathin films from very dilute solutions of a good solvent. We show in

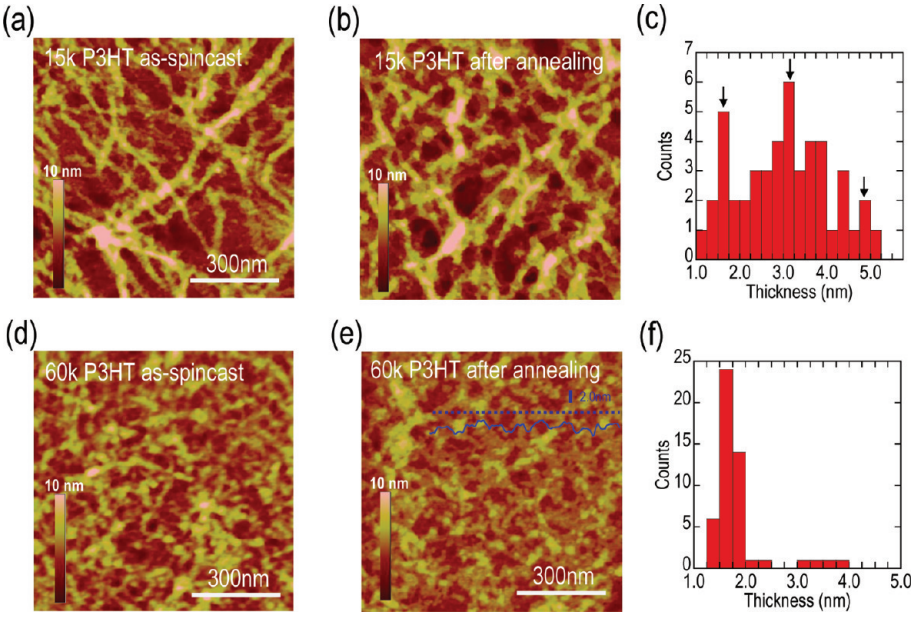

Figure 9. 1 × 1 μm AFM images of 15 nm-thick rrP3HT films spin-cast from a chlorobenzene:mesitylene (1:9 v/v) mixture. (a) Pristine film with apparent M_n of 15k and (b) after annealing and cooling from the liquid-crystalline phase. (c) Histogram of step heights measured at the edges of the nanoribbons. Arrows denote the (100)-spacing and its multiples. (d) Pristine film with apparent M_n of 60k and film (e) after annealing and cooling from the liquid-crystalline phase. (f) Histogram of the step heights measured at the edges of the terraces. *z*-scale is 10 nm.

dx.doi.org/10.1021/ma201165y |*Macromolecules* 2011, 44, 9692–9702

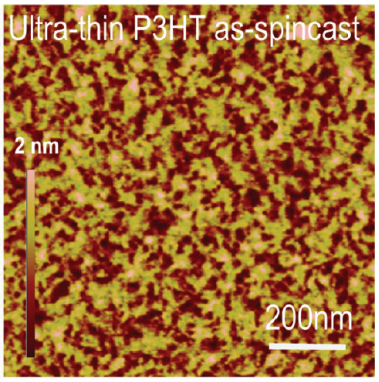

Figure 10. 1 × 1 μm AFM image of a 2-nm-thick rrP3HT film with apparent M_n of 60k spin-cast from chlorobenzene onto HMDS-treated silicon oxide surface.

Supporting Information S3 the typical nodular film morphology of the rrP3HT spin-cast from CB as has been widely observed in the literature. We have separately checked first using variable-temperature wide-angle X-ray scattering and polarizing optical microscopy that rrP3HT has a LC phase[44] between 440−500 K.

A suitable borderline solvent for rrP3HT was established through its solvatochromic effect at a concentration of 2−3 mg mL^{-1}. rrP3HT was dissolved at 80 °C into aliquots of a good solvent (CB) mixed with a poor solvent (mesitylene) at different proportions, and cooled to room temperature. A good solvent is indicated by an orange solution that persists over several days. A poor solvent turns black within minutes and precipitates the polymer. The borderline solvent turns dark red due to the formation of π-stacks which remains dispersed for hours. In this way a 1:9 v/v mixture of CB: mesitylene was found to be a borderline solvent.

Two different samples of rrP3HT with apparent M_w* of 15k and 60k were dissolved into this solvent mixture, and spin-cast to give 15 nm-thick films on HMDS-treated Si wafers. These films were then annealed at 465 K for 10 min and cooled through T_k at 10 K min^{-1}. The 15k rrP3HT film gives nanoribbons together with elongated monolayer and multilayers. The lamellar order becomes significantly improved after anneal and cool from the LC phase (Figure 9b). Clear lamellae can be discerned with widths of 20−40 nm, and a step height of 1.6 nm which corresponds to the (100)-spacing, and its multiples (Figure 9c). Similarly the 60k rrP3HT film also shows lamellar order in the as-deposited state, which improves after annealing. The *as*-deposited film exhibits a similar nanoplatelet morphology (Figure 9d) as PBTTT, which evolves to the distinctive monolayer-terraced morphology (Figure 9e) with uniform 1.6 nm step heights as evidenced by the distinctive layering of the image (see also the line profile) and the emergence of a dominant mode in the step-height histogram (Figure 9f). Although the lateral widths of these features are finer than those of PBTTT, it is indisputable that the monolayer-terraced morphology that is so characteristic of extended-chain π-stacks have now been induced in rrP3HT films over a wide range of MWs.

Finally, we show the morphology of a 2-nm ultrathin film of rrP3HT spin-cast from the good solvent CB onto HMDS-treated silicon oxide surface in Figure 10. It is clear that excellent lamellar order can be produced here even without thermal annealing. This is consistant with our dilute π-stacking meachnism as explained in the concluding paragraph of section IIIG.

Therefore, it can be firmly concluded that it is not really a particular II-stacking motif of PBTTT or a crystallization of the alkyl side chains that is responsible for the superior lamellar order observed in its annealed films, but the formation of unentangled extended-chain 2D π-stacked aggregates in dilute solutions that deposit parallel to the film plane. This can be achieved using borderline solvents for practical film thicknesses, or in good solvents at high dilution for ultrathin films. This work here reiterates the central role that solvent processing play in determining the final supramolecular organization of the polymer chains.

■ ASSOCIATED CONTENT

Supporting Information. Experimental details including **P22** and **rrP3HT** solution UV−vis absorption spectra, histogram of the widths from atomic force microscopy, atomic force microscopy images. This material is available free of charge via the Internet at http://pubs.acs.org.

■ AUTHOR INFORMATION

Corresponding Author
*E-mail: chmcll@nus.edu.sg.

■ ACKNOWLEDGMENT

This work was funded by MOE (Project R-143-000-431-112). We also thank Bibin Thomas Anto for performing the ^{1}H NMR, and Peter Ho for technical discussions and insights.

■ REFERENCES

(1) Prosa, T. J.; Winokur, M. J.; Moulton, J.; Smith, P.; Heeger, A. J. *Synth. Met.* **1993**, *55*−*57*, 370–377.

(2) Sirringhaus, H.; Brown, P. J.; Friend, R. H.; Nielsen, M. M.; Bechgaard, K.; Langeveld-Voss, B. M. W.; Spiering, A. J. H.; Janssen, R. A. J.; Meijer, E. W.; Herwig, P.; de Leeuw, D. M. *Nature* **1999**, *401*, 685–688.

(3) Aasmundtveit, K. E.; Samuelsen, E. J.; Guldstein, M.; Steinsland, C.; Flornes, O.; Fagermo, C.; Seeberg, T. M.; Pettersson, L. A. A.; Inganäs, O.; Feidenhans'l, R.; Ferrer, S. *Macromolecules* **2000**, *33*, 3120–3127.

(4) Causin, V.; Marega, C.; Marigo, A.; Valentini, L.; Kenny, J. M. *Macromolecules* **2005**, *38*, 409–415.

(5) Meille, S. V.; Romita, V.; Caronna, T.; Lovinger, A. J.; Catellani, M.; Belobrzeckaja, L. *Macromolecules* **1997**, *30*, 7898–7905.

(6) Zhuo, J. M.; Zhao, L. H.; Png, R. Q.; Wong, L. Y.; Chia, P. J.; Tang, J. C.; Sivaramakrishnan, S.; Zhou, M.; Ou, E. C. W.; Chua, S. J.; Sim, W. S.; Chua, L. L.; Ho, P. K. H. *Adv. Mater.* **2009**, *21*, 4747–4752.

(7) McCulloch, I.; Heeney, M.; Bailey, C.; Genevicius, K.; MacDonald, I.; Shkunov, M.; Sparrowe, D.; Tierney, S.; Wagner, R.; Zhang, W.; Chabinyc, M. L.; Kline, R. J.; McGehee, M. D.; Toney, M. F. *Nat. Mater.* **2006**, *5*, 328–333.

(8) Chabinyc, M. L.; Toney, M. F.; Kline, R. J.; McCulloch, I.; Heeney, M. *J. Am. Chem. Soc.* **2007**, *129*, 3226–3237.

(9) Ihn, K. J.; Moulton, J.; Smith, P. *J. Polym. Sci., Part B: Polym. Phys.* **1993**, *31*, 735–742.

(10) Kline, R. J.; McGehee, M. D.; Kadnikova, E. N.; Liu, J.; Fréchet, J. M. J. *Adv. Mater.* **2003**, *15*, 1519–1522.

(11) Zen, A.; Pfaum, J.; Hirschmann, S.; Zhuang, W.; Jaiser, F.; Asawapirom, U.; Rabe, J. P.; Scherf, U.; Neher, D. *Adv. Funct. Mater.* **2004**, *14*, 757–764.

(12) Kline, R. J.; McGehee, M. D.; Kadnikova, E. N.; Liu, J.; Fréchet, J. M. J.; Toney, M. F. *Macromolecules* **2005**, *38*, 3312–3319.

(13) Zhang, R.; Li, B.; Iovu, M. C.; Jeffries-EL, M.; Sauvé, G.; Cooper, J.; Jia, S.; Tristram-Nagle, S.; Smilgies, D. M.; Lambeth, D. N.; McCulloch, R. D.; Kowalewski, T. *J. Am. Chem. Soc.* **2006**, *128*, 3480–3481.
(14) Chang, J. F.; Sun, B.; Breiby, D. W.; Nielsen, M. M.; Sölling, T. I.; Giles, M.; McCulloch, I.; Sirringhaus, H. *Chem. Mater.* **2004**, *16*, 4772–4776.
(15) Chang, J. F.; Clark, J.; Zhao, N.; Sirringhaus, H.; Breiby, D. W.; Andreasen, J. W.; Nielsen, M. M.; Giles, M.; Heeney, M.; McCulloch, I. *Phys. Rev. B* **2006**, *74*, 115318–1−12.
(16) Liu, J.; Arif, M.; J., Z.; Khondaker, S. I.; Zhai, L. *Macromolecules* **2009**, *42*, 9390–9393.
(17) Wu, Z. Y.; Petzold, A.; Henze, T.; Thurn-Albrecht, T.; Lohwasser, R. H.; Sommer, M.; Thelakkat, M. *Macromolecules* **2010**, *43*, 4646–4653.
(18) Mena-Osteritz, E.; Meyer, A.; Langeveld-Voss, B. M. W.; Janssen, R. A. J.; Meijer, E. W.; Bäuerle, P. *Angew. Chem., Int. Ed.* **2000**, *39*, 2680–2684.
(19) Samitsu, S.; Shimomura, T.; Heike, S.; Hashizume, T.; Ito, K. *Macromolecules* **2008**, *41*, 8000–8010.
(20) Kim, D. H.; Park, Y. D.; Jang, Y.; Kim, S.; Cho, K. *Macromol. Rapid Commun.* **2005**, *26*, 834–839.
(21) Merlo, J. A.; Frisbie, C. D. *J. Polym. Sci., B: Polym. Phys.* **2003**, *41*, 2674–2680.
(22) Malik, S.; Nandi, A. K. *J. Polym. Sci., B: Polym. Phys.* **2002**, *40*, 2073–2085.
(23) Hugger, S.; Thomann, R.; Heinzel, T.; Thurn-Albrecht, T. *Colloid Polym. Sci.* **2004**, *2004*, 932–938.
(24) Wang, S.; Tang, J. C.; Zhao, L. H.; Png, R. Q.; Wong, L. Y.; Chia, P. J.; Chan, H. S. O.; Ho, P. K. H.; Chua, L. L. *Appl. Phys. Lett.* **2008**, *93*, 162103–1−3.
(25) Zhao, L. H.; Png, R. Q.; Zhuo, J. M.; Guo, H.; Tang, J. C.; Wong, L. Y.; Friend, R. H.; Chua, L. L.; Ho, P. K. H. Manuscript submitted, 2011.
(26) DeLongchamp, D. M.; Kline, R. J.; Jung, Y.; Lin, E. K.; Fischer, D. A.; Gundlach, D. J.; Cotts, S. K.; Moad, A. J.; Richter, L. J.; Toney, M. F.; Heeney, M.; McCulloch, I. *Macromolecules* **2008**, *41* (15), 5709–5715.
(27) Kline, R. J.; DeLongchamp, D. M.; Fischer, D. A.; Lin, E. K.; Richter, L. J.; Chabinyc, M. L.; Toney, M. F.; Heeney, M.; McCulloch, I. *Macromolecules* **2007**, *40*, 7960–7965.
(28) Brocorens, P.; Van Vooren, A.; Chabinyc, M. L.; Toney, M. F.; Shkunov, M.; Heeney, M.; McCulloch, I.; Cornil, J.; Lazzaroni, R. *Adv. Mater.* **2009**, *21*, 1193–1198.
(29) Heeney, M.; Bailey, C.; Genevicius, K.; Shkunov, M.; Sparrowe, D.; Tierney, S.; McCulloch, I. *J. Am. Chem. Soc.* **2005**, *127*, 1078–1079.
(30) Zhao, L. H.; Png, R. Q.; Zhuo, J. M.; Tang, J. C.; Ho, P. K. H.; Chua, L. L. Manuscript submitted 2011.
(31) Ho, P. K. H.; Chua, L. L.; Dipankar, M.; Gao, X. Y.; Qi, D. C.; Wee, A. T. S.; Chang, J. F.; Friend, R. H. *Adv. Mater.* **2007**, *19*, 215–221.
(32) Hoven, C. V.; Dang, X. D.; Coffin, R. C.; Nguyen, T. Q.; Bazan, G. C. *Adv. Mater.* **2010**, *22*, E63–E66.
(33) Lee, K. L.; Ma, W. L.; Brabec, C. J.; Yuen, J.; Moon, J. S.; Kim, J. Y.; Lee, K. H.; Bazan, G. C.; Heeger, A. J. *J. Am. Chem. Soc.* **2008**, *130*, 3619–3623.
(34) McCulloch, I.; Heeney, M.; Chabinyc, M. L.; DeLongchamp, D. M.; Kline, R. J.; Cölle, M.; Duffy, W.; Fischer, D. A.; Gundlach, D.; Hamadani, B.; Hamilton, R.; Richter, L.; Salleo, A.; Shkunov, M.; Sparrowe, D.; Tierney, S.; Zhang, W. *Adv. Mater.* **2009**, *21*, 1091–1109.
(35) Umeda, T.; Tokito, S.; Kumaki, D. *J. Appl. Phys.* **2007**, *101*, 054517–1−5.
(36) Sperling, L. H. *Introduction to physical polymer science*, 3rd ed.; Wiley-interscience: New York, 2001.
(37) Gedde, U. W. *Polymer physics*; Chapman & Hall: London, 1995.
(38) Huber, K.; Bantle, S.; Lutz, P.; Burchard, W. *Macromolecules* **1985**, *18*, 1461–1467.
(39) Heffner, G. W.; Pearson, D. S. *Macromolecules* **1991**, *24*, 6295–6299.
(40) Rughooputh, S. D. D. V.; Hotta, S.; Heeger, A. J.; Wudl, F. *J. Polym. Sci., B: Polym. Phys.* **1987**, *25*, 1071–1078.
(41) Inganäs, O.; Salaneck, W. R.; Österholm, J. E.; Laakso, J. *Synth. Met.* **1988**, *22*, 395–406.
(42) Yoshino, K.; Nakajima, S.; Park, D. H.; Sugimoto, R. *Jpn. J. Appl. Phys.* **1988**, *27*, L716–718.
(43) Inganäs, O.; Gustafsson, G.; Salaneck, W. R.; Österholm, J. E.; Laakso, J. *Synth. Met.* **1989**, *28*, C377–384.
(44) Tashiro, K.; Ono, K.; Minagawa, Y.; Kobayashi, M.; Kawai, T.; Yoshino, K. *J. Polym. Sci. B, Polym. Phys.* **1991**, *29*, 1223–1233.
(45) Zerbi, G.; Chierichetti, B.; Inganäs, O. *J. Chem. Phys.* **1991**, *94*, 4646–4658.
(46) Tashiro, K.; Minagawa, Y.; Kobayashi, K.; Morita, S.; Kawai, T.; Yoshino, K. *Synth. Met.* **1993**, *55*−*57*, 321–328.
(47) Ho, P. K. H.; Kim, J. S.; Tessler, N.; Friend, R. H. *J. Chem. Phys.* **2001**, *115*, 2709–2720.
(48) DeLongchamp, D. M.; Kline, R. J.; Lin, E. K.; Fischer, D. A.; Richter, L.; Lucas, L. A.; Heeney, M.; McCulloch, I.; Northrup, J. E. *Adv. Mater.* **2007**, *19*, 833–837.
(49) Wong, L. Y.; Png, R. Q.; Silva, F. B. S.; Chua, L. L.; Repaka, D.; Chen, S.; Gao, X. Y.; Ke, L.; Chua, S. J.; Wee, A. T. S.; Ho, P. K. H. *Langmuir* **2010**, *26*, 15494–15507.
(50) Campoy-Quiles, M.; Etchegoin, P. G.; Bradley, D. D. C. *Phys. Rev. B* **2005**, *72*, 045209–1−15.